Geophys. J. Int. (1996) **125**, 768–780

Source investigation of a small event using empirical Green's functions and simulated annealing

F. Courboulex,[1] J. Virieux,[1] A. Deschamps,[1] D. Gibert[2] and A. Zollo[3]

[1] *Géosciences Azur, Université de Nice-Sophia Antipolis, Rue A. Einstein, 06560 Valbonne, France*
[2] *Géosciences, Rennes* I, *Avenue Général Leclerc, 35042 Rennes cédex, France*
[3] *Departmento di Geofisca e Vulcanologia, Università di Napoli, Italy*

Accepted 1996 January 23. Received 1996 January 23; in original form 1994 October 21

SUMMARY

We propose a two-step inversion of three-component seismograms that (1) recovers the far-field source time function at each station and (2) estimates the distribution of co-seismic slip on the fault plane for small earthquakes (magnitude 3 to 4). The empirical Green's function (EGF) method consists of finding a small earthquake located near the one we wish to study and then performing a deconvolution to remove the path, site, and instrumental effects from the main-event signal.

The deconvolution between the two earthquakes is an unstable procedure: we have therefore developed a simulated annealing technique to recover a stable and positive source time function (STF) in the time domain at each station with an estimation of uncertainties. Given a good azimuthal coverage, we can obtain information on the directivity effect as well as on the rupture process. We propose an inversion method by simulated annealing using the STF to recover the distribution of slip on the fault plane with a constant rupture-velocity model. This method permits estimation of physical quantities on the fault plane, as well as possible identification of the real fault plane.

We apply this two-step procedure for an event of magnitude 3 recorded in the Gulf of Corinth in August 1991. A nearby event of magnitude 2 provides us with empirical Green's functions for each station. We estimate an active fault area of 0.02 to 0.15 km^2 and deduce a stress-drop value of 1 to 30 bar and an average slip of 0.1 to 1.6 cm. The selected fault of the main event is in good agreement with the existence of a detachment surface inferred from the tectonics of this half-graben.

Key words: Green's functions, inversion, Patras, source time functions.

INTRODUCTION

The empirical Green's function (EGF) method proposed by Hartzell (1978) shows that recordings of small earthquakes contain the propagation characteristics necessary for modelling large nearby earthquakes, and therefore yield empirical Green's functions that are more appropriate than the synthetic seismograms generated by modelling the wave propagation in an inadequately known structure. Mueller (1985) used this concept to recover the source time function (STF) of a larger event by deconvolving the small-earthquake seismograms from those of the larger one, thus removing path, site and instrumental effects.

This method has been widely applied to a large number of earthquakes ranging from moderate ($M = 4$) to very large ($M = 7$) events, using local network data (Mueller 1985; Frankel & Wennerberg 1989; Mori & Hartzell 1990; Hough *et al.* 1991), strong motion data (Hartzell 1978; Fukuyama & Irikura 1986), as well as regional and teleseismic body and surface waveforms (Hartzell 1989; Kanamori *et al.* 1992; Velasco, Ammon & Lay 1994).

The applicability of the EGF method to a wide range of earthquakes is still an open question; for example, the sensitivity to the thickness of the seismogenic layer may prohibit the use of this method for very large earthquakes (Scholz 1982), while, for very small earthquakes, the influence of lithological structures is not clearly understood (Feignier 1991).

In this study, we apply the EGF method to earthquakes of magnitude ~ 3 or ~ 4 using the EGF given by events of magnitude ~ 2. The deconvolution procedure to be applied between the two earthquakes is an unstable process. A range of different techniques, including both time-domain and frequency-domain deconvolution, have been proposed in the literature to tackle this problem (Helmberger & Wiggins 1971; Lawson & Hanson 1974; Zollo, Capuano & Singh 1995).

We propose a new time-analysis tool based on a simulated annealing inversion to solve this problem and to recover a positive and stable STF. The method that we have developed is a two-step inversion. The first step consists of finding a stable and positive STF by simulated annealing deconvolution (SAD) at each available station. The computed far-field STF may differ from one station to another because STFs incorporate the directivity effect of the source. In the second step, we first use the method developed by Zollo & Bernard (1991b), which is based on the construction of isochrons in order to constrain the active fault-plane dimensions for the main shock. Then, we perform an inversion of slip distribution over this fault plane using deconvolved far-field STFs deduced by the SAD method at each station. We obtain a detailed description of the rupture process for small earthquakes assuming a circular rupture model with a constant rupture velocity.

This kind of detailed waveform study requires a dense local network composed of seismic stations with a dynamic range high enough to avoid saturated signals for the main event and with a sensitivity great enough to record signals of the small event.

We applied this two-step inversion method to a set of seismograms from a dense seismic network deployed during 1991 July and August in the Patras area of the Gulf of Corinth, Greece. Many events of magnitude 1.5 to 3.5 were recorded by three-component seismographs. This area has been the subject of extensive studies (Rigo 1994; Le Meur 1994), which have provided us with precise locations and well-constrained focal mechanisms. We studied in detail an event that occurred in the northern part of the Gulf, and obtained interesting results relating to the rupture process of this 100 m sized event and the determination of the active fault plane.

After a presentation of the EGF assumptions, we will give a detailed explanation of the SAD that we propose, and the two-step inversion method that we use.

EMPIRICAL GREEN'S FUNCTIONS

For a small event occurring in the same period as and close to a larger one, waves reaching a given station follow the same ray paths, and the site response, which includes local propagating effects near the station as well as instrumental response, is the same for both events. If the two events have the same focal mechanism, we may assume a linear scaling between the two earthquakes; this is the basic self-similar assumption of the EGF method.

With this hypothesis, we can use recordings of the small earthquake as the empirical Green's function of the larger one (Mueller 1985) in order to remove the source radiation pattern and, path, site and instrumental effects of the signal by deconvolution at each station, and to recover the far-field source time function.

The two selected events must not be too different in size with respect to the propagation distance so that the recorded signal of the small event can be used as the Green's function for any point of the fault associated with the large earthquake. Only global time shifts estimated in the far-field approximation are taken into account as we move along the fault. In addition, the smaller earthquake must be small enough that its far-field source time function can be approximated by a Dirac function. In reality, the small-event source function has a finite duration, and therefore a high-frequency-limited spectrum. This high-frequency limit is represented by the corner frequency of the small event and corresponds to the maximum resolution that we can obtain on the large-event rupture process.

The EGF method assumes that the two events have the same hypocentre. Consequently, waves that radiate from the nucleation points of the two events should cross exactly the same medium. In reality the two events are slightly shifted in space, and a heterogeneity in the source region can be detected by only one of the events. This is a restriction of the EGF method, but the resulting error is smaller than the one that would result from using a calculated Green's function.

Nevertheless, for each type of phase the time shift of waves coming from the source area will be the same, whatever the complexity of the propagation path. Since we pick the initial pulse on the STF manually at each station, and considering that this initial pulse is radiated by the rupture nucleation, we synchronize seismograms at each station at an absolute time. In so doing, we remove the temporal effect of any possible small difference in location of the two events.

THE DECONVOLUTION PROBLEM

The first problem we have to solve is the recovery of the apparent STF at a given station. We then need to deconvolve the seismogram of the smaller earthquake from that of the larger one.

The signals used for convolution are the empirical Green's function and the assumed source time function, which have nearly the same number of points in time. The associated deconvolution, where the STF must be estimated from the recorded seismogram for each station, is therefore an unstable time-analysis problem, although the convolution is a linear operation. Spectral deconvolution (Mueller 1985; Mori 1993; Ammon, Velasco & Lay 1993) has been widely used and different filtering strategies (Helmberger & Wiggins 1971) have been performed to recover a nearly positive source time function. Positive constraints on the source function make the problem even more complex, although several techniques exist to solve a linear problem under positivity constraints (Lawson & Hanson 1974).

Since the empirical Green's function in this study has nearly the same duration as the source function that we are looking at, the matrix associated with the convolution is very sensitive to the propagation of numerical errors, and often has a condition number greater than 1000 for 100 parameters. This means that errors in the estimated source time function are not bounded by perturbations of the convolution matrix built from the empirical Green's function. Moreover, estimation of the STFs are very sensitive to the cut-off that can be selected to stabilize the result, i.e. to the *a priori* information or damping that we include in the source-time-function retrieval procedure.

In order to control and minimize these effects we propose an inverse technique for solving the deconvolution problem. This is based on the iterative solution of the forward problem and estimation of a misfit function. For each station, the misfit is computed by comparing the synthetic signals, obtained by convolution of the EGF with an assumed STF for the large shock, with the observed recording of the same event. Each iteration is driven by a numerical technique called simulated annealing, which we describe below. Additionally, we shall use the three components of the signal to estimate errors on the results using a cross-validation technique.

SIMULATED ANNEALING DECONVOLUTION (SAD)

Annealing consists of heating a solid until thermal stresses are released and then freezing it very slowly to reach the state of lowest energy where the total crystallization is obtained. If the cooling is too fast, a metastable glass can be formed, corresponding to a local minimum of energy.

Simulated annealing is a numerical method proposed by Kirkpatrick, Gellat & Vecchi (1983) and Cerny (1985), analogous to the process of physical annealing, to obtain the global minimum of a multiparameter function. In the same way as for the physical process, the cooling must be slow enough to prevent the system from being trapped into a local minimum. This cooling procedure is a compromise between local convergent methods and global Monte Carlo methods.

The inversion method will be used to recover the STF by deconvolution and then to retrieve the slip distribution over the earthquake fault plane. The method consists of solving the forward problem many times instead of trying to perform the inversion of the linear matrix associated with the deconvolution problem numerically. Because this algorithm requires intensive forward modelling, we must design a fast method to compute the forward problem in order to have an inverse algorithm that is sufficiently powerful. In this inversion the parameters we wish to determine are the amplitudes of the STF for each point in time.

The simulated annealing is a two-loop procedure. The first loop consists of perturbing the model randomly and solving the forward problem, and the second loop involves decreasing a parameter T (temperature). This parameter enables the procedure to be highly non-linear at the beginning and to become slowly linearized. If the decrease in temperature is properly chosen, the method permits us to avoid local minima of the function and allows us to reach the global minimum in a reasonable number of iterations. The temperature, T, plays the same role as the noise variance, and decreasing the temperature during the cooling schedule is equivalent to gradually increasing the influence of the data on the choice of the new model (Tarantola 1987).

In this study we use a 'heat bath' technique, which is more efficient at low temperature than the classical Metropolis procedure (Metropolis *et al.* 1953). This fast technique has been developed by Creutz (1980) and applied by Rothman (1986) to seismic static corrections and Gilbert & Virieux (1991) to electromagnetic imaging.

The misfit function is defined by an L_2 norm,

$$S(k) = \sum_{i=1}^{I} [A_{obs}(i) - A_{syn}(i)]^2, \tag{1}$$

where I is the number of time points, i is the current point, $A_{obs}(i)$ is the value of the observed signal at the station and $A_{syn}(i)$ is the value of the synthetic one estimated by convolution. First, the starting temperature, T_i, is chosen equal to the average of the misfit function, $S(n)$, obtained over 100 iterations, plus the standard deviation, $sd(\,)$:

$$T_i = \langle S(n) \rangle + sd(S(n)). \tag{2}$$

We then calculate at each discretized time step i of the STF the misfit function $S(K)$ associated with every possible amplitude value, k, while keeping other values of the STF fixed. The speed of the forward modelling loop is increased by modifying only those terms associated with the current point. The probability of acceptance, P_a, can be defined for each value of amplitude, k, for a given point in time, depending on the misfit value and the actual temperature, as:

$$P_a(k) = \frac{\exp(-S(k)/T)}{\sum_{k=1}^{K} \exp(-S(k)/T)}. \tag{3}$$

From this probability distribution, one can guess the amplitude at the current point, i. Then, the next point in time of the STF is considered and the whole procedure is undertaken again. One loop is when all points have been taken into account. An average of ten loops at the same temperature is enough to make the result insensitive to the sequential selection of points inside the solution. We have verified that reversing the order of the selection of points gives us the same solution with the same number of loops. After these ten loops, which correspond to one iteration of the simulated annealing procedure, we decrease the temperature (Fig. 1).

When the temperature is high, the probability distribution is almost insensitive to the misfit function and any value can be chosen. When the temperature decreases, few models remain acceptable, and when the system is frozen, only the solution providing the smallest misfit function is kept.

One difficulty of numerical simulated annealing, as is the case for the corresponding physical technique, is the protocol for cooling the temperature. If one imposes a cooling that is too slow, retrieval of the solution becomes very expensive, whereas a cooling that is too quick may trap the solution into a local minimum (Kirkpatrick *et al.* 1983). We have used the strategy proposed by Huang, Romeo & Sangiovanni-Vincentelli (1986) and used by Gilbert & Virieux (1991) where the cooling is made at a constant thermodynamic speed, λ. We must verify that the average energy at iteration $n+1(\langle S(n+1) \rangle)$ is below the average energy at iteration $n(\langle S(n) \rangle)$ by λ times the standard deviation of the energy at iteration n:

$$\langle S(n+1) \rangle = \langle S(n) \rangle - \lambda sd(S(n)). \tag{4}$$

Then, the cooling law is:

$$T(n+1) = T(n) \exp[-\lambda T(n)/sd(S(n))]. \tag{5}$$

In practice, we have taken a value of λ around 0.1, and the number of iterations at a constant temperature equal to 10. This gives a good estimate of the average energy and the standard deviation.

Another problem that has to be solved is the determination of the final temperature. This can be done simply, by decreasing the temperature until the system is totally frozen. In this case, only one solution is retained. In order to take into account the possible non-uniqueness of solution, and also the uncertainties contained in the data itself, we propose the decreasing of the temperature to a critical value equal to the noise variance of the data. This value is calculated using the three components of the signal and cross-validation theory, as described in Courboulex, Virieux & Gilbert (1996).

At this temperature, we perform a large number of iterations and keep the entire set of models. In the following example we will use the average of these solutions and the standard deviation that permits us to estimate uncertainties on the STF obtained.

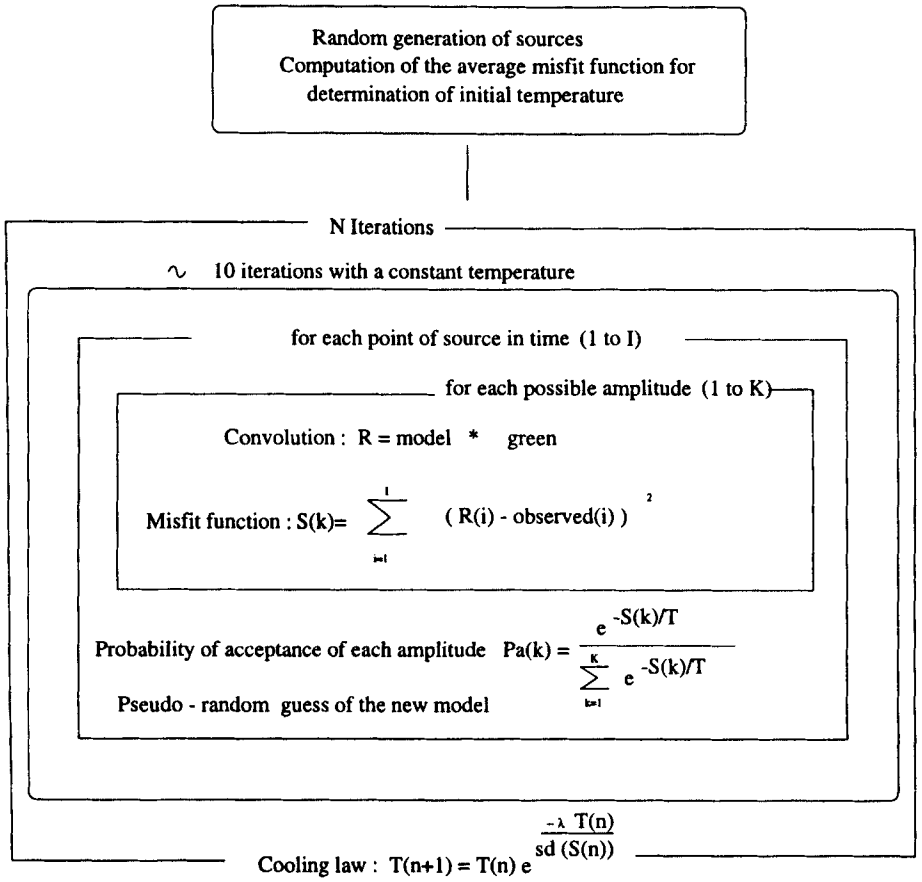

Figure 1. Diagram of the heat-bath algorithm.

Let us now present the two-step method that we propose in order to recover the spatio–temporal source of an earthquake.

A TWO-STEP INVERSION METHOD

The far-field body-wave displacement for a given fault-plane geometry is obtained by the classical representation equation (Aki & Richards 1980):

$$U^c(\mathbf{x}, t) = \int_{\text{fault}} G(\mathbf{x}, t; \mathbf{r}_0) * \Delta\dot{u}(\mathbf{r}_0, t - T_c(\mathbf{x}, \mathbf{r}_0))\, d\Sigma, \qquad (6)$$

where Δu is the scalar slip function, $\mathbf{x}$ and $\mathbf{r}_0$ denote the receiver and source position, respectively, c indicates the wave type (P or S waves) and T_c is the traveltime. The far-field Green's function G is taken as an empirical Green's function. The dot sign denotes the time derivative, while the asterisk denotes convolution.

The first step is the reconstruction of the global contribution of the whole fault plane at a given station by the simulated annealing deconvolution, as explained above, that estimates the STF. We must solve the following equation:

$$U^c(t) = G(t) * \text{STF}(t), \qquad (7)$$

and recover the apparent source time function at a given station.

Because the medium complexity has been extracted by deconvolution, the STF at each station represents only the source complexity in space and in time as if the medium were homogeneous. The most obvious effect will be the directivity effect, which modifies the STF shape at different stations, especially if these are well distributed in azimuth around the fault plane.

Once the far-field source time functions are obtained at each station, we propose to back-propagate them onto the earthquake fault plane to determine its space–time slip distribution. In order to investigate the spatio-temporal slip dependence at the source, we need to solve the following equation for the slip velocity, $\Delta\dot{u}$:

$$\text{STF}(\mathbf{x}, t) = \int_{\text{fault}} \Delta\dot{u}(\mathbf{r}_0, t - (T_c(\mathbf{x}, \mathbf{r}_0) + T_r(\mathbf{r}_0))\, d\Sigma, \qquad (8)$$

where T_r is the rupture time while T_c is the wave-propagation time. Propagation is performed in a homogeneous medium because propagation effects in a complex medium have been removed by deconvolution of EGF according to eq. (7). Thus, the representation integral is reduced to a summation of the contribution of several subfaults delayed by rupture time plus propagation time estimated inside a homogeneous medium.

We discretize the fault plane on a regular grid and use the simulated annealing technique for recovering the slip velocity amplitude, $\Delta\dot{u}$, on the fault (Fig. 2). The direction of the slip velocity is assumed constant and defined by the specified focal mechanism of the main shock.

In summary, the first step consists of finding the appropriate STF at each station by using the EGF method, and the second step is the estimation of the slip distribution on the fault plane.

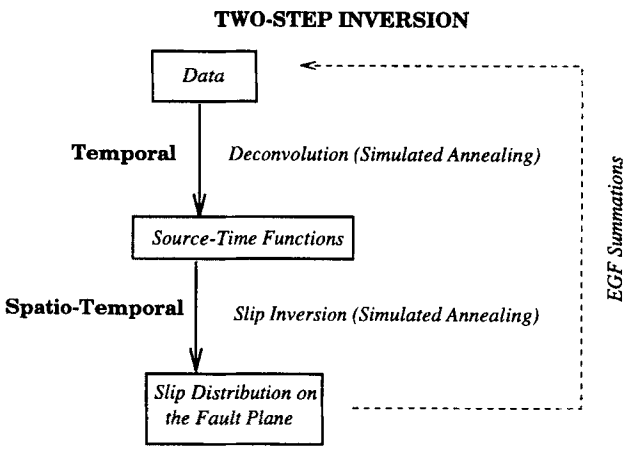

Figure 2. Two-step inversion procedure for recovering the slip distribution.

With this method, it is possible to estimate physical quantities on the fault plane, such as ruptured surface and stress drop, and to provide arguments to discriminate between the two nodal planes based on either a misfit function or on a realistic slip distribution. Finally, in order to check the global accuracy of the spatio–temporal slip distribution obtained with our two-step inversion, we perform the empirical Green's function summation over the fault plane for all stations, in one step, using eq. (6) directly.

DATA ANALYSIS

The Aegean region is one of the most seismically active regions of the Mediterranean basin (Le Pichon & Angelier 1987; Jackson & McKenzie 1988). The Gulf of Corinth is a well-studied example of active extensional tectonics (Jackson *et al.* 1982; Ori 1989; Hatzfeld *et al.* 1993; Lyon-Caen *et al.* 1994). This gulf is recognized as a half-graben, bounded to the south by major normal faults, with no evidence of active rupture on the northern side.

A seismic network was deployed in 1991 July and August, around the Gulf of Corinth. 60 short-period (2 Hz and 5 s) portable digital stations were installed in the Patras–Aigion region and recorded over 5000 events with a sampling frequency ranging from 125 to 200 Hz. We have worked on a set of 600 well-constrained events of 1991 August recorded by the three-component stations shown in Fig. 3.

Because the medium in the Patras region is complex and not yet well known, we wanted to use empirical Green's functions to model path effects on seismograms. We defined criteria to find earthquakes for which this technique can be applied. In the search for potential candidates of earthquake couples, an automatic selection of the available data set was performed using the following criteria:

(1) the difference in magnitude must be larger or equal to 1;
(2) the difference in hypocentre location must be smaller than 2 km;
(3) both events must be recorded at a minimum of three common stations;
(4) the stations must be well distributed in azimuth around the epicentre.

The last two criteria were difficult to satisfy because the smaller events were often recorded by very few stations located near the hypocentre. For these stations, seismograms of the main event are likely to be saturated. Then, a visual inspection of each selected couple of events was required, in order to eliminate saturated traces and to check the similarity of the waveforms and the focal mechanisms of the two events. The number of event candidates was small enough to make this task feasible.

We selected two events that met these criteria. The main earthquake occurred on 1991 August 2 on the northern coast of the Gulf of Corinth. It was recorded by a large number of stations in the local network: 18 three-component stations and 16 one-component instruments. Its duration magnitude has been estimated as 3. Its focal mechanism was determined by Rigo (1994) using *P*-wave polarities and *S*-wave polarizations by applying the method developed by Zollo & Bernard (1991a). The solution is a normal-fault mechanism. One nodal plane is pseudo-vertical and oriented east–west with a southerly dip (strike = 088°, dip = 73°) and the other is almost horizontal, with a shallow northerly dip (strike = 300°, dip = 20°). Both planes are possible fault planes and lead to different geodynamic explanations of this area. The pseudo-vertical plane can be interpreted as an antithetic fault of the southern system, and the pseudo-horizontal plane might be explained as a décollement zone. No surface ruptures were observed, and choosing which plane was active is a difficult task, although it is a key question for the tectonic interpretation. In this study we attempt to resolve this point with a detailed analysis of the source coherence for the two supposed fault planes.

The small earthquake chosen as the empirical Green's function occurred on 1991 August 16. Its location was close to the main event and its magnitude was estimated at 2. It was recorded by 12 stations, four of which were three-component stations. We relocated it with respect to the main event by using the master-event technique, and found an interevent distance of 1.8 km. The focal solution is almost identical to the main-event nodal fault planes (Fig. 4). The waveform similarity of both events and likeness of focal mechanisms leads us to consider the August 16 event as a possible empirical Green's function for the August 2 event.

Three stations were available for our study. This number is small compared to the large number of events and the dense distribution of stations at our disposal. It highlights the fact that high-dynamic-range stations are necessary to avoid saturation of traces and to record very small events. Stations MARM, SERG and LIMN were azimuthally well distributed around the epicentre at distances of 15, 16 and 18 km, respectively (see Fig. 3). Seismograms of both events recorded by the three stations are shown in Fig. 5. The study is mainly performed on *S*-wave signals because shear waves enhance the detection of source directivity.

SOURCE-TIME-FUNCTION RETRIEVAL

On each component of the seismogram and for each station, a time window of 1 s around the identified *S* pulse is extracted and tapered by 10 per cent at both ends. We have applied a filter to the raw signal because of the decimation required by the simulated annealing technique. The filter depends on the number of points imposed on the source. The cut-off frequency of this implicit low-pass filter is chosen to be around the value

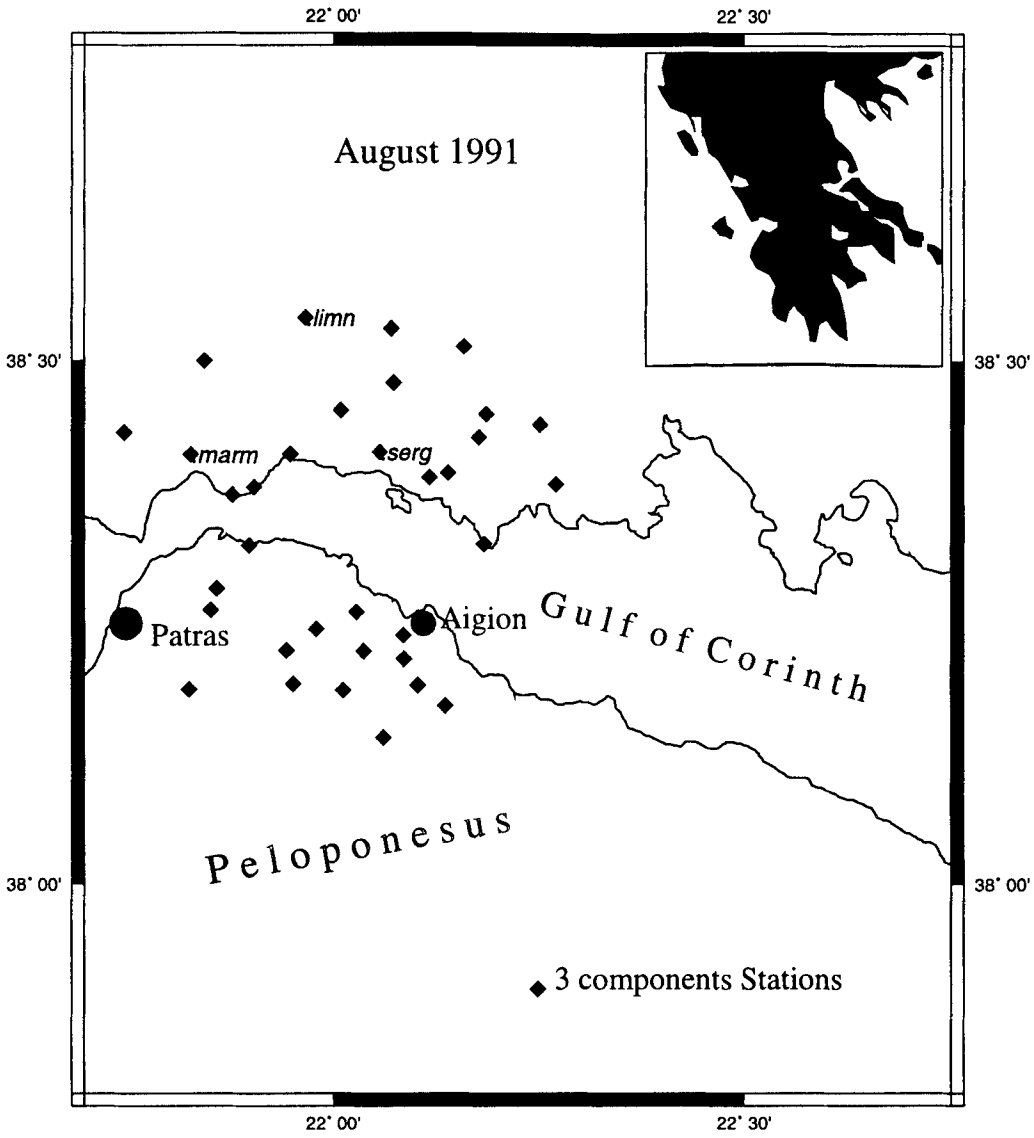

Figure 3. Three-component seismic stations deployed in the Gulf of Corinth near Patras during July and August 1991.

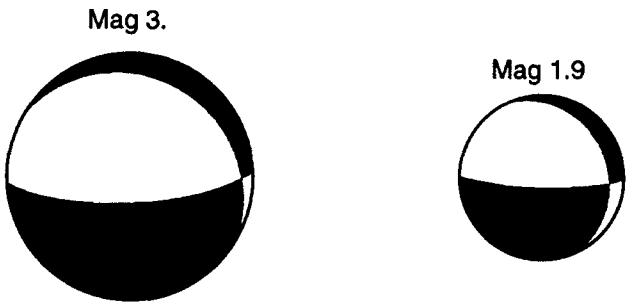

Figure 4. Focal mechanisms of the two events after Rigo (1994).

of the corner frequency of the smaller earthquake. We recall that the initial time of the picking is quite arbitrary, and, consequently, the initial time of the apparent source time function will also be arbitrary.

The functional space of STF must be defined. The selected time step is related to the corner frequency of the smallest event. From the spectra, we found that the highest possible frequency would be 30 Hz, limiting our time discretization, Δt, to a value equal to, or higher than, 0.03 s. The time step, Δt, strongly influences the smoothing of the signal, but several numerical experiments with different Δt showed a good stability of the STF envelope.

The maximum positive amplitude is chosen by trial and error. From an initially relatively high value, we decrease the maximum permissable amplitude after a few tests. The amplitude step depends mainly on the required precision for the STF. Of course, a large number of values increases the convergence time of the solution when using the simulated annealing deconvolution, as explained previously.

We use the three components of the signal together in order to obtain a set of STFs that best fit the three components, and to estimate errors on the STF obtained. Fig. 6 shows the estimated apparent source time functions bounded by uncertainties, and Fig. 7, the observed and synthetic signals at each station for each component. Synthetics were obtained by convolution of the average STF solution and the empirical Green's function of each component. We immediately observe

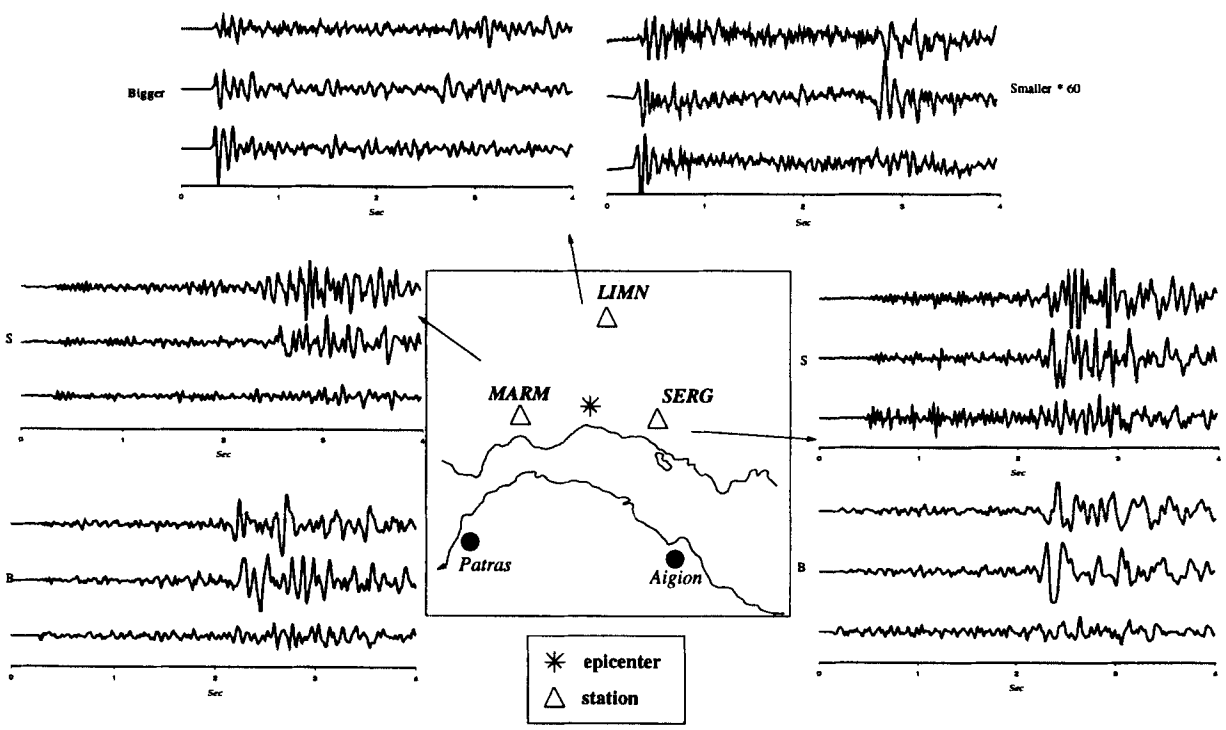

Figure 5. Three-component velocity seismograms for station LIMN, SERG and MARM for the main earthquake (B) and for the smaller one (S). Seismograms of the smaller event are scaled by a factor of 60 with respect to the seismograms of the main shock.

that the fit is worst on the vertical components. This can be easily explained by the scarse information from *S* waves on the vertical component. The amplitude of *S* waves is low and, consequently, contributes very little to our calculation of the L_2 norm misfit function.

We observe an important difference between the three apparent source time functions. While the main peak source duration at station LIMN is about 0.1 s, the duration at station SERG is about 0.2 s and that at station MARM is about 0.25 s. The seismic rupture seems, therefore, to move towards the north-east.

SPATIO-TEMPORAL SOURCE MODEL

Isochron construction

In order to constrain the functional model space of possible slip-velocity distribution, we should first define the possible active region for each fault plane. We use isochron construction, as defined by Bernard & Madariaga (1984) and Spudich & Frazer (1984) for constraining the final extension of the rupture area (Zollo & Bernard 1991b). Starting from the nucleation point, the rupture propagates with a constant velocity, and slip is assumed to have a step-like shape in time. Radiation from points on the fault which contribute to the *S*-wave pulse at time t along the seismogram belongs to a so-called isochron. These isochrons are geometrically defined by

$$t = T_r(\mathbf{r}_0, \mathbf{r}_1) + T_c(\mathbf{r}_0, \mathbf{x}), \tag{9}$$

where $\mathbf{r}_0$ and $\mathbf{r}_1$ denote the nucleation and isochron points and $\mathbf{x}$ denotes the receiver position. T_r represent the rupture time while T_c is the wave-propagation time. The traveltimes are inferred assuming a constant rupture-propagation velocity. If we draw the isochrons for the final extension of the rupture at each station, the intersection of the three isochrons delimits a zone that must contain the real fracture area. This area depends on the rupture velocity we consider for the calculation. We chose an upper limit of rupture velocity equal to the shear-wave velocity. Because the rupture propagates at the same speed as the energy propagates along the fault plane, the rupture velocity is lower than the Rayleigh velocity and, consequently, lower than the shear-wave velocity. We have, therefore, defined the maximum possible ruptured area. We discretize the fault plane into several subfaults, and the point-source approximation is imposed at the subfault scale.

For each of the two possible fault planes, the active fracture area has a different shape. Fig. 8 shows a rupture propagation towards the north-north-east for the two fault planes. The shape and the area of the ruptured zone is very different in the two cases. For the near-vertical plane, the rupture zone has an elongated shape and may cover an area of 1 km^2; for the horizontal plane, the rupture area is almost circular and much smaller (0.4 km^2). The up-dip rupture propagation obtained for the vertical plane is consistent with the observation that many earthquakes initiate near the bottom of the source area and then rupture propagates towards the surface (Sibson 1982; Mori & Hartzell 1990).

Slip inversion

In order to produce a more refined solution of the slip-velocity distribution, we can use the amplitude information and perform an inversion with the simulated annealing method to determine the slip distribution on the two possible fault planes. In this inversion, the rupture velocity is kept constant and a circular rupture model is imposed. The beginning of rupture is taken

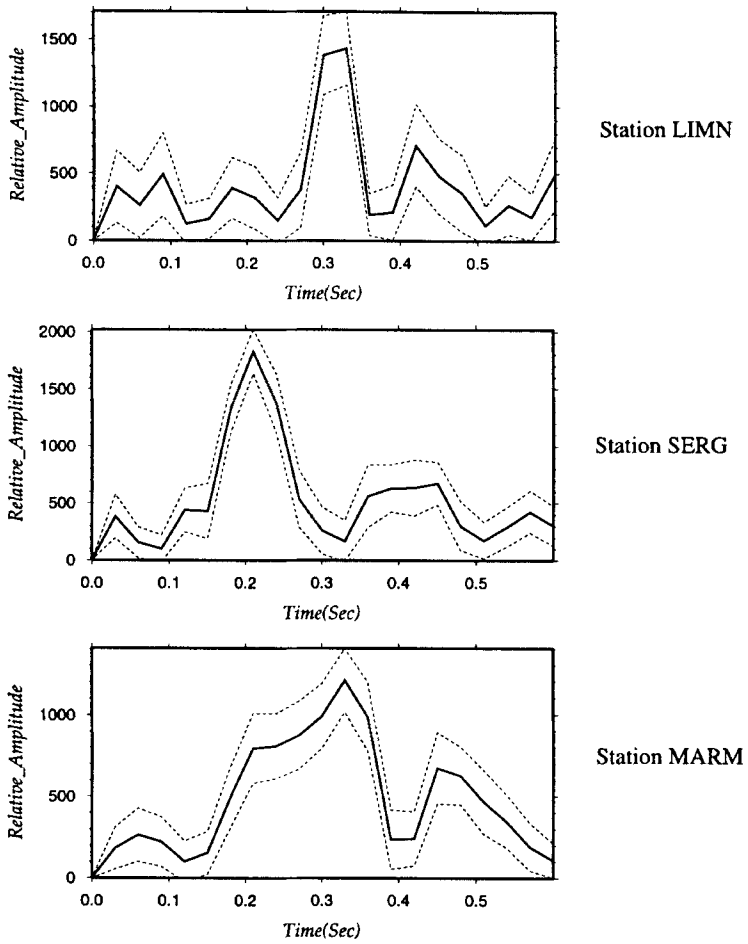

Figure 6. Deconvolved STF at the three stations obtained by deconvolution of the three components together. The bold line represents the average solution and dashed lines the error estimates.

as the beginning of the main pulse identified on the STF. Consequently, we only require a relative time-scale.

The space discretization Δx obeys the inequality $\Delta x \leq V_{\text{rmin}} * \Delta t$, where V_{rmin} is the minimum possible rupture velocity (Herrero 1994) and Δt is the same time-step as used for the deconvolution process. The maximum slip velocity is estimated by trial and error starting from initially high values and decreasing them through numerical tests.

The misfit function for this inversion is expressed as follows:

$$C = \sum_{k=1}^{3} \sum_{n=1}^{N} (\text{STF}_{\text{obs}}(k, n) - \text{STF}_{\text{syn}}(k, n))^2, \qquad (10)$$

where the index k is over the three stations and index n is over the number of points of the STF. The term STF_{obs} represents the source time functions calculated by deconvolution using expression (7) at a given station, and STF_{syn}, that obtained by summation of slip velocities on the fault plane using eq. (8).

As with deconvolution, we have developed a procedure to estimate only the perturbation of the misfit function for the modified subfault, reducing the computation time for the simulated annealing process. Moreover, we perform the forward problem very efficiently because instead of calculating the synthetic seismogram at each station, we need only sum the slip-velocity amplitudes delayed by the rupture and propagation durations. This is the advantage of the two-step inversion that we propose. In a small number of iterations, we reach a good fit of the three apparent source time functions.

Another parameter has to be taken into account in this model: the rise time of each subfault source time function. We first assumed a step-like STF, which means that, in theory, a point on the fault reaches its maximum slip instantaneously. Because of numerical discretization, the rise time we considered is a multiple of Δt. We also considered models where the rise time is longer for each subfault: then, the radiation emitted from a given point on the fault plane involves a higher number of points in time on the seismograms.

RESULTS

We attempt to solve the problem using different rupture velocities and different rise-time durations. Results of the minimum-misfit values obtained for the two fault planes are shown in Fig. 9. A minimum value is obtained for a rupture velocity of 3 km s^{-1} and a rise time equal to twice Δt. For both possible fault planes, we invert the final slip-velocity distribution with the simulated annealing method. The time step Δt is equal to 0.03 s and the spatial step Δx to 100 m.

In Figs 10 and 11 the distribution of cumulative slip at three different rupture times is shown for subvertical and subhorizontal fault planes, respectively. The planes are oriented

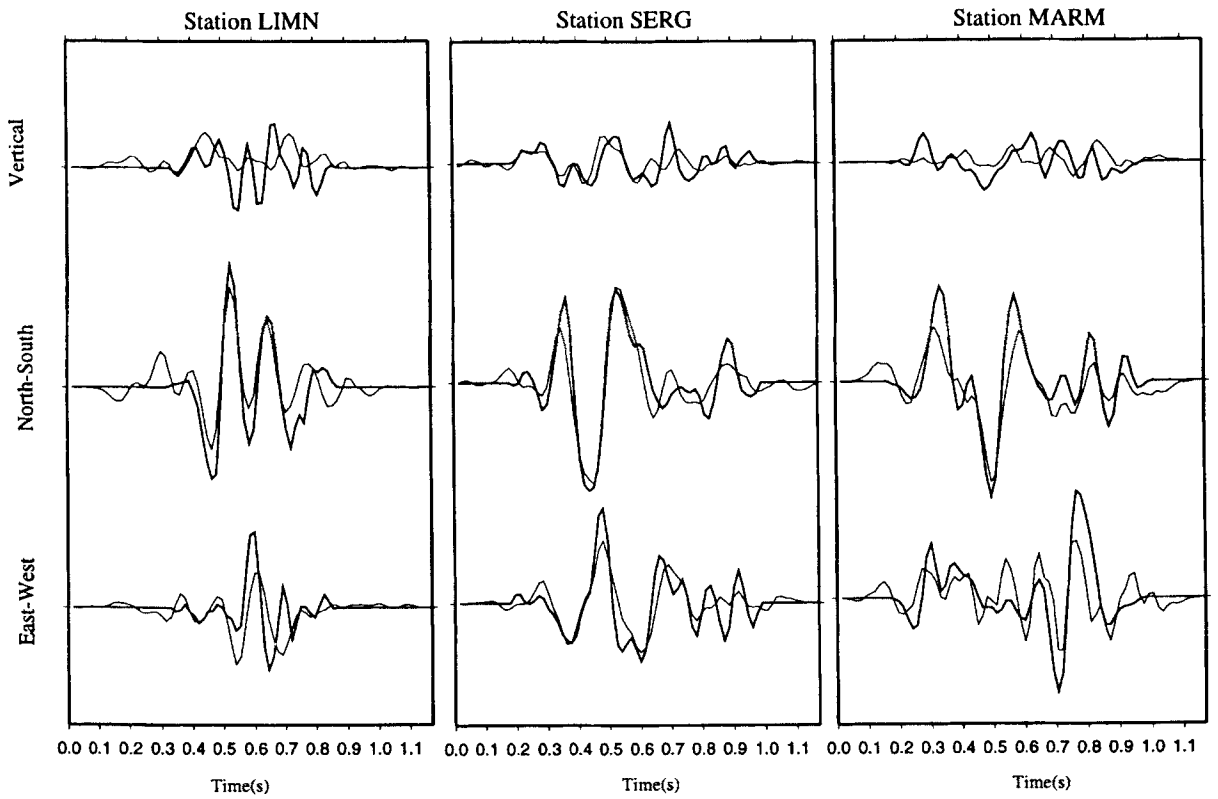

Figure 7. Observed (bold lines) and synthetic (thin lines) seismograms obtained by convolution of the average STF and the EGF at each station. Vertical scale is the same for each component of a station.

along the strike and dip directions. The origin time, which is associated with the nucleation, is represented by a black diamond. These results show a possible rupture history. Along both planes, the total active area is between 500 and 1100 m^2, which is much smaller than the value estimated with the limit-isochron construction, and the rupture direction is towards the north-north-east.

Along the subvertical plane, the spatial evolution of the rupture is not continuous, with a jump from the nucleation point to the maximum area of slip and almost no slip velocity between them. The distribution of the final slip on the sub-horizontal plane shows a more credible rupture pattern. In this case, the rupture propagation is continuous from the nucleation point to the edges of the fractured area. The consistency of this last solution and the generally smaller value of the misfit function (see Fig. 9) suggest that the subhorizontal fault plane was probably the active plane.

In order to obtain an absolute value for slip (the values on Figs 10 and 11 were scaled by a slip factor), the seismic moment, M_0, of the event was set equal to the moment derived from the moment–magnitude relation (Thatcher & Hanks 1973):

$$\log M_0 = 1.5M_L + 16.0. \quad (11)$$

The computation of seismic moments by Wajeman *et al.* (1995) from six stations gives an average value of 1×10^{20} dyne cm. We have also estimated the seismic moment using the expression from Boatwright (1980); this gives a value of about 0.8×10^{20} dyne cm. Using the definition of the seismic moment,

$$M_0 = \mu DA, \quad (12)$$

where μ, the rigidity, is set equal to 3×10^{11} dyne cm^2, we can deduce a total average slip, D, over the fault plane. The static stress drop is given by Kanamori & Anderson (1975) as:

$$\Delta\sigma = C\mu(D/L), \quad (13)$$

where C is a geometrical factor of about 1.0 and L is the fault dimension, quantities estimated by our analysis. Results for stress drop, total active area and average total slip are shown in Table 1 for the two possible fault planes and two different rise times.

The values are bounded by the uncertainties of the estimation of the effective active area on the fault. This gives us values of the average total slip of between 0.1 and 1 cm and a stress drop of between 1 and 10 bar for a rise time equal to Δt, and a stress drop that can reach 30 bar for a rise time equal to twice Δt. We do not show results for longer rise times because the misfit function is not satisfactory.

DISCUSSION AND CONCLUSION

The values that we obtain depend on the kinematic model that we use. We apply a model where the energy is radiated by discontinuities in the slip velocity, assuming a constant rupture velocity and the same rise time for each point. We chose the best value of this velocity using the misfit function. With a smaller value, the area involved would have been smaller and the stress drop higher.

We have also seen in Table 1 that the inversion is sensitive to the chosen rise-time value. Indeed, when the radiation duration of a given point is very short, a higher number of

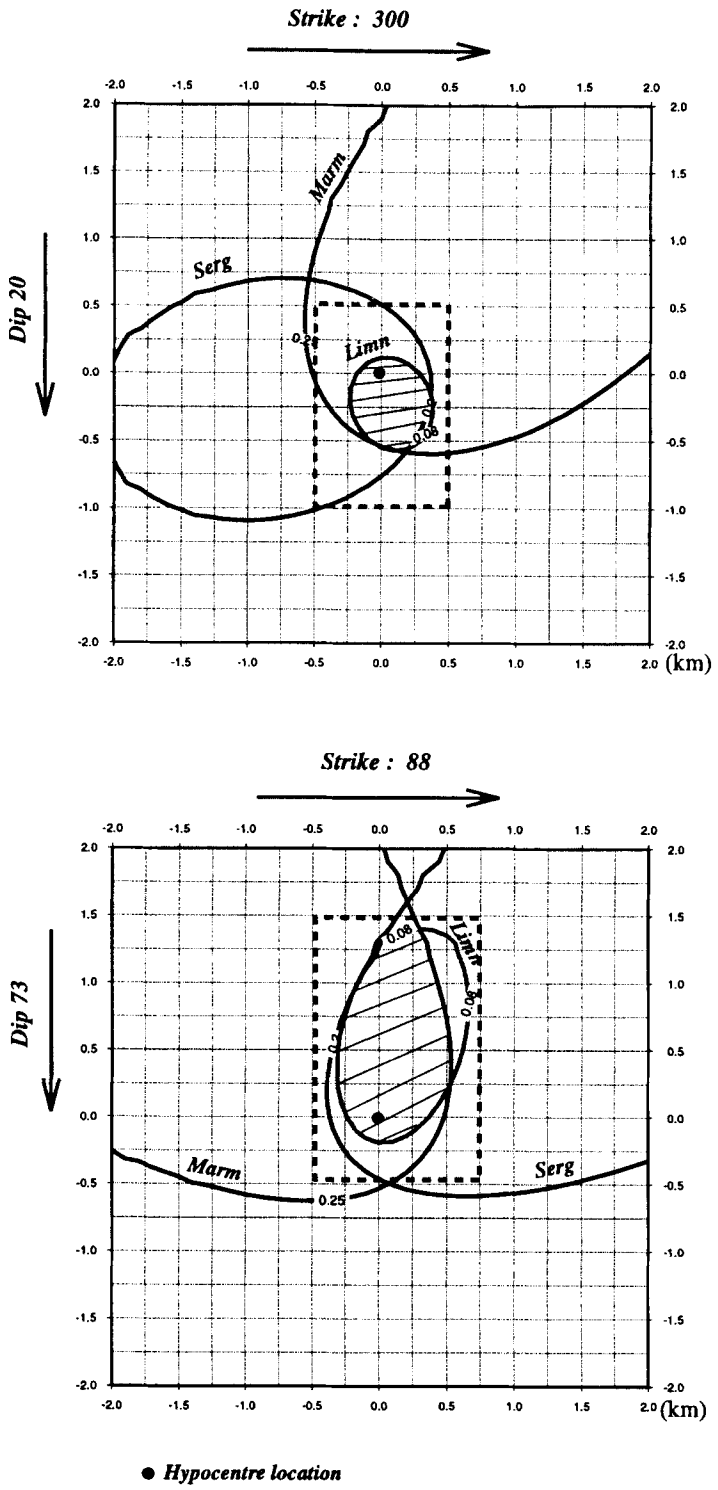

Figure 8. Limit isochrons over the two fault planes. The rupture velocity is taken as the shear-wave velocity. Zones within dashed frames represent the two areas that will be used for inversion.

active points is needed to fit the data and consequently the active fault plane has to be larger and the stress drop deduced is lower. For each case the stress drop remains very low; this is consistent with other determinations for events of a similar size (Mori & Hartzell 1990).

Our results concerning the choice of the fault plane are in good agreement with the seismotectonic deductions from the Patras Gulf area (Rigo 1994). Indeed, the distribution of aftershocks leads us to believe that there is a subhorizontal sliding zone in this area. Conclusions about the large-scale tectonics cannot be obtained just by looking at small-scale rupture phenomena, but these can provide an additional argument in favour of a particular interpretation.

In the present study, only three stations were available, but

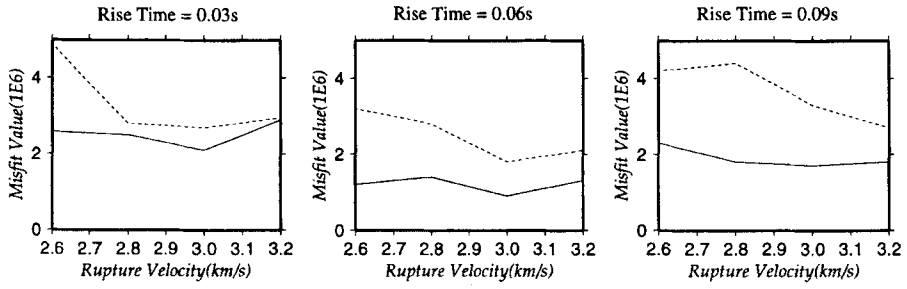

Figure 9. Misfit function for different rupture velocities and three different rise-time values. Results are shown for the subvertical fault plane (dashed line) and the subhorizontal fault plane (continuous line).

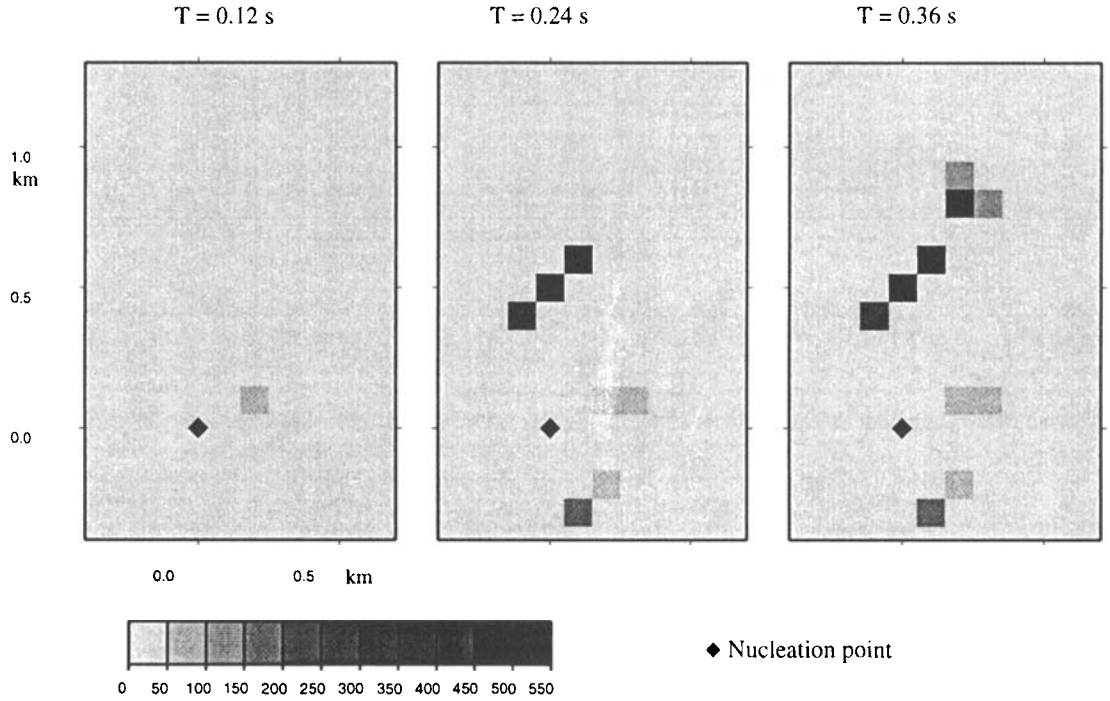

Figure 10. Cumulative slip distribution on the subvertical fault plane at three different rupture times obtained for a rupture velocity of 3 km s^{-1} and a rise time equal to 0.06 s. The scale represents a slip factor.

they were especially well distributed in azimuth. This analysis shows what kind of results this method can provide. Given a larger number of data, we could complicate the model that we use for the forward problem. For example, it is possible to consider a different rise-time value for each subfault STF, or a non-constant rupture velocity.

The inversion method that we propose provides an analysis tool that can be used to investigate the rupture details of small events. Using seismograms of a smaller earthquake as empirical Green's functions eliminates the effects of propagation through complex media, and makes it possible to separate propagation and source factors on seismograms. The simulated annealing method that we developed for deconvolution enabled us to recover a positive and stable source time function at each station with an error estimation. From these functions, we were able to estimate the slip distribution on given fault planes in an efficient way. This two-step inversion is simpler in terms of computational effort and more stable than inverting complicated seismograms in one step. In fact, we can check the spatial variation of the information we gather with the apparent STF functions before starting the second-step procedure.

This method enabled us to highlight directivity effects and provided arguments for choosing which of the two fault planes determined by the focal mechanism was the active one. A good azimuthal station coverage is essential in this study, and the higher the number of stations we have, the better the resolution of the problem.

With the simple kinematic rupture model that we employ we can deduce the average active area of the fault and a static stress-drop value. These values are compatible with a hypothesis of self-similar scaling, even for small earthquakes (Aki & Richards 1980), but we can not overrule a possible breaking of scaling laws for small earthquakes from our study. For example, the hypothesis of a constant fault area for small earthquakes and then a decreasing stress drop cannot be inferred from our work.

ACKNOWLEDGMENTS

We are grateful to D. Hatzfeld and H. Lyon-Caen, who directed the field experiment, as well as to K. Macropoulos for his help. We thank the people who worked on the 1991 Patras data set,

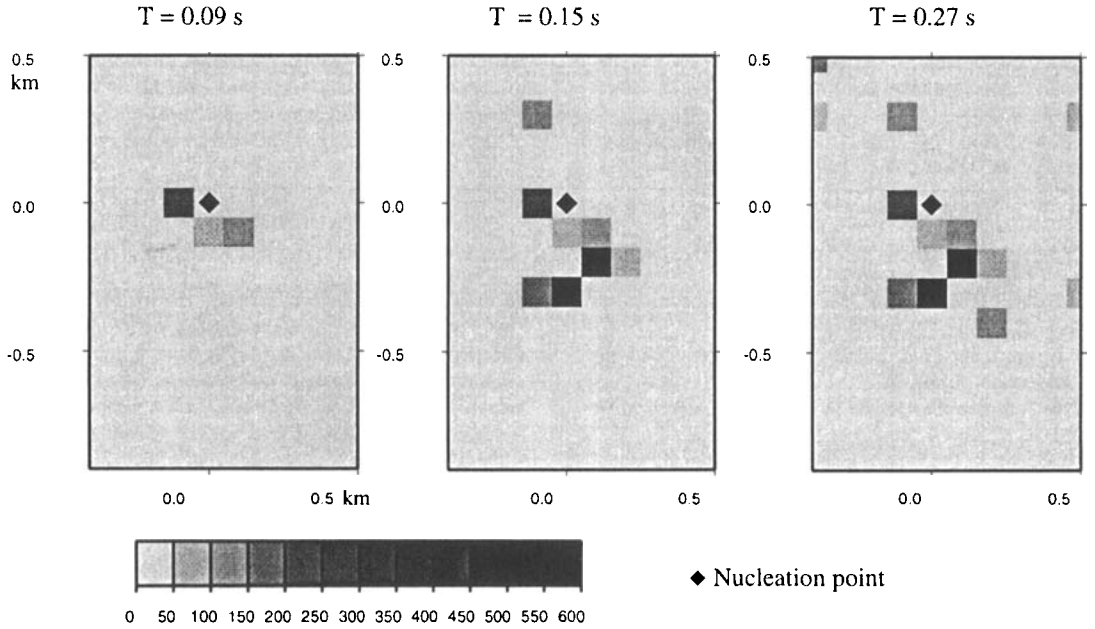

Figure 11. Cumulative slip distribution on the subhorizontal fault plane at three different rupture times obtained for a rupture velocity of 3 km s^{-1} and a rise time equal to 0.06 s. The scale represents a slip factor.

Table 1.

		Area(km^2)	Average slip(cm)	Stress drop(bar)
Rise-time=Δt	Sub-vertical plane	$0.1 < A < 0.25$	$0.12 < D < 0.33$	$0.7 < \Delta\sigma < 3.3$
	Sub-horizontal plane	$0.05 < A < 0.15$	$0.22 < D < 0.66$	$1.7 < \Delta\sigma < 9$
Rise-time=$2 \times \Delta t$	Sub-vertical plane	$0.03 < A < 0.12$	$0.27 < D < 1.1$	$2.3 < \Delta\sigma < 19$
	Sub-horizontal plane	$0.02 < A < 0.1$	$0.3 < D < 1.6$	$2.8 < \Delta\sigma < 33$

M.P. Bouin, H. Le Meur and especially A. Rigo, for accurate focal mechanism determinations, C. Wajeman for moment calculations and H. Lyon-Caen for her help in retrieving data. We would also like to thank O. Scotti for a critical review and the two anonymous reviewers for their accurate remarks. This study was supported by DRM of the French Ministry for Environment (SRETIE 90392), INSU/CNRS through the programmes PNRN 1994 and DBT-Instabilités and the Ministry of National Education through Jeune Equipe RUaDE. Publication no. 2 de l'Unité CNRS-UNSA Géosciences Azur.

REFERENCES

Aki, K. & Richards, P., 1980. *Quantitative seismology: theory and methods,* W.H. Freeman, San Francisco, CA.

Ammon, C., Velasco, A. & Lay, T., 1993. Rapid estimation of rupture directivity: application to the 1992 Landers (Ms = 7.4) and Cape Mendocino (Ms = 7.2) California earthquakes, *Geophys. Res. Lett.,* **20,** 97–100.

Bernard, P. & Madariaga, R., 1984. A new asymptotic method for the modelling of near-field accelerograms, *Bull. seism. Soc. Am.,* **74,** 539–557.

Boatwright, J., 1980. Spectral theory for circular seismic sources: simple estimates of source dimension, dynamic stress drop and radiated energy, *Bull. seism. Soc. Am.,* **70,** 1–28.

Cerny, V., 1985. A thermodynamical approach to the travelling salesman problem, *J. Optimisation Theory Appl.,* **45,** 41–51.

Courboulex, F., Virieux, J. & Gilbert, D., 1996. On the use of cross-validation theory and simulated annealing for deconvolution, *Bull. seism. Soc. Am.,* in press.

Creutz, M., 1980. Monte Carlo study of quantized SU(2) gauge theory, *Phys. Rev.,* **21,** 2308–2315.

Feignier, B., 1991. How geology can influence scaling relations, *Tectonophysics,* **197,** 41–53.

Frankel, A. & Wennerberg, L., 1989. Microearthquake spectra from the Anza, California, seismic network: site response and source scaling, *Bull. seism. Soc. Am.,* **79,** 581–609.

Fukuyama, E. & Irikura, K., 1986. Rupture process of the 1983 Japan Sea (akita-oki) earthquake using a waveform inversion method, *Bull. seism. Soc. Am.,* **76,** 1623–1640.

Gibert, D. & Virieux, J., 1991. Electromagnetic imaging and simulated annealing, *J. geophys. Res.,* **96,** 8057–8067.

Hartzell, S., 1978. Earthquake aftershocks as Green's functions, *Geophys. Res. Lett.,* **5,** 1–4.

Hartzell, S., 1989. Comparison of seismic waveform inversion results for a rupture history of a finite fault: application to the 1986 North Palm Springs, California, earthquake, *J. geophys. Res.,* **94,** 7515–7534.

Hatzfeld, D. *et al.,* 1993. Subcrustal microearthquake seismicity and fault plane solutions beneath the Helenic arc, *J. geophys. Res.,* **98,** 9861–9870.

Helmberger, D. & Wiggins, R., 1971. Upper mantle structure of the mid-western United States, *J. geophys. Res.,* **76,** 3229–3245.

Herrero, A., 1994. Paramétrisation spatio temporelle et spectrale dessources sismiques: application au risque sismique, *Thèse de doctorat,* University of Paris 6, France.

Hough, S., Seeber, L., Lerner-Lam, A., Armbruster, J. & Guo, H., 1991. Empirical Green's functions analysis of Loma Prieta aftershocks, *Bull. seism. Soc. Am.,* **81,** 1737–1753.

Huang, M., Romeo, F. & Sangiovanni-Vincentelli, A., 1986. An efficient general cooling schedule for simulated annealing, *Proc. IEEE Int. Conf. Computer-Aided Design, Santa Clara,* 381–384.

Jackson, J. & McKenzie, D., 1988. The relationship between plate motions and seismic moment tensors, and the rates of active deformation in the Mediterranean and Middle East, *Geophys. J. Int.,* **93,** 45–73.

Jackson, J., Gagnepain, J., Housman, G., King, G., Papadimitriou, P., Soufleris, C. & Virieux, J., 1982. Seismicity, normal faulting and the geomorphological development of the gulf of Corinth (Greece): the Corinth earthquakes of February and March 1981, *Earth planet. Sci. Lett.*, **57,** 377–397.

Kanamori, H. & Anderson, D.L., 1975. Theorical basis of some empirical relations in seismology, *Bull. seism. Soc. Am.*, **65,** 1073–1095.

Kanamori, H., Thio, H., Dreger, D., Hauksson, E. & Heaton, T., 1992. Initial investigation of the Landers California earthquake of the 28 June 1992 using TERRAscope, *Geophys. Res. Lett.*, **19,** 2267–2270.

Kirkpatrick, S., Gellat, J. & Vecchi, M., 1983. Optimization by simulated annealing, *Science,* **220,** 671–680.

Lawson, C.L. & Hanson, R., 1974. *Solving Least Squares Problems,* Prentice-Hall, Englewood Cliffs, NJ.

Le Meur, H., 1994. Tomographie 3D de la croûte dans la région de Patras (Grèce), *PhD thesis,* University of Paris 7, France.

Le Pichon, X. & Angelier, J., 1987. The Hellenic arc and trench system: a key to the evolution of the Eastern Mediterranean area, *Tectonophysics,* **60,** 1–42.

Lyon-Caen, H. *et al.*, 1994. Seismotectonics and deformation of the Gulf of Corinth, *EOS, Trans. Am. geophys. Un.,* **75,** 116.

Metropolis, N., Rosenbluth, A., Rosenbluth, M., Teller, A. & Teller, E., 1953. Equation of state calculation by fast computing machines, *J. Chem. Phys.,* **21,** 1087–1092.

Mori, J., 1993. Fault plane determination for three small earthquakes along the San Jacinto fault, California: search for cross faults, *J. geophys. Res.,* **98,** 711–723.

Mori, J. & Hartzell, S., 1990. Source inversion of the 1988 Upland, California, earthquake: determination of a fault plane for a small event, *Bull. seism. Soc. Am.,* **80,** 507–518.

Mueller, C., 1985. Source pulse enhancement by deconvolution of an empirical Green's function, *Geophys. Res. Lett.,* **12,** 33–36.

Ori, G., 1989. Geologica history of the extensional basin of the Gulf of Corinth, Greece, *Geology,* **17,** 918–921.

Rigo, A., 1994. Etude sismotectonique et géodésique du golfe de Corinthe (Grèce), *PhD Thesis,* University of Paris, France.

Rothman, D., 1986. Automatic estimation of large residual statics corrections, *Geophysics,* **51,** 332–346.

Scholz, C., 1982. Scaling laws for large earthquakes: consequences for physical models, *Bull. seism. Soc. Am.,* **72,** 1–14.

Sibson, R., 1982. Fault zone models, heat flow and the depth distribution of earthquakes in the continental crust of the United States, *Bull. seism. Soc. Am.,* **72,** 151–163.

Spudich, P. & Frazer, L., 1984. Use of ray theory to calculate high frequency radiation from earthquake sources having spatially variable rupture velocity and stress drop, *Bull. seism. Soc. Am.,* **74,** 2061–2082.

Tarantola, A., 1987. Inverse problem theory: methods for data fitting and model parameter estimation, Elsevier, Amsterdam.

Thatcher, W. & Hanks, T., 1973. Source parameters of southern California earthquakes, *J. geophys. Res.,* **78,** 8547–8576.

Velasco, A., Ammon, C. & Lay, T., 1994. Empirical Green function deconvolution of broadband surface waves: rupture directivity of the 1992 Landers, California (Mw = 7.3), earthquake, *Bull. seism. Soc. Am.,* **84,** 735–750.

Wajeman, C., Bard, P., Hatzfeld, D., Diagourtas, D., Makropulos, K. & Gariel, J.C., 1995. Experimental tests on the empirical Green's Function methods, *Proc. 5th Int. Conf. in Seismic Zonation,* Nice, France.

Zollo, A. & Bernard, P., 1991a. Fault mechanisms from near source data: joint inversion of *S* polarizations and *P* polarities, *Geophys. J. Int.,* **104,** 441–451.

Zollo, A. & Bernard, P., 1991b. How does an asperity break? New elements from the waveform inversion of accelerograms for the 2319 UT, October 15, 1979, Imperial Valley aftershock, *J. geophys. Res.,* **96,** 549–573.

Zollo, A., Capuano, P. & Singh, S., 1995. Use of small earthquake records to determine the source function of a larger earthquake: an alternative method and an application, *Bull. seism. Soc. Am.,* **85,** 1249–1256.